Structural Transition in a Fluid of Spheroids: A Low-Density Vestige of Jamming

A. P. Cohen,[1] S. Dorosz,[2] A. B. Schofield,[3] T. Schilling,[2] and E. Sloutskin[1,*]
[1]Physics Department and Institute of Nanotechnology and Advanced Materials, Bar-Ilan University, Ramat-Gan 5290002, Israel
[2]Research Unit for Physics and Materials Science, Université du Luxembourg, L-1511 Luxembourg, Luxembourg
[3]School of Physics and Astronomy, University of Edinburgh, Edinburgh EH9 3FD, United Kingdom
(Received 4 November 2015; published 1 March 2016)

A thermodynamically equilibrated fluid of hard spheroids is a simple model of liquid matter. In this model, the coupling between the rotational degrees of freedom of the constituent particles and their translations may be switched off by a continuous deformation of a spheroid of aspect ratio t into a sphere ($t = 1$). We demonstrate, by experiments, theory, and computer simulations, that dramatic nonanalytic changes in structure and thermodynamics of the fluids take place, as the coupling between rotations and translations is made to vanish. This nonanalyticity, reminiscent of a second-order liquid-liquid phase transition, is not a trivial consequence of the shape of an individual particle. Rather, free volume considerations relate the observed transition to a similar nonanalyticity at $t = 1$ in structural properties of jammed granular ellipsoids. This observation suggests a deep connection to exist between the physics of jamming and the thermodynamics of simple fluids.

DOI: 10.1103/PhysRevLett.116.098001

The thermodynamics of a fluid of simple spheres is well-known and almost completely understood [1,2]. However, the constituents of real matter are typically nonspherical. Their translational degrees of freedom are coupled to their rotations [3]. A system of spheroids, ellipsoids of revolution, is arguably the simplest model of matter, where such a coupling exists. This model has recently been realized in colloidal and granular matter experiments, providing an important insight onto the local bulk structure of fluids [4,5] and jammed packings [6]. While a very good agreement between experiment and theory has been achieved for the fluids [5,7], these studies dealt with only one specific particle aspect ratio, $t = 1.6$. The dependence of the fluid structure on the aspect ratio of the constituent particles has not been tested, so that the fundamental role played in these fluids by rotational degrees of freedom remains unknown. The understanding of jammed packings of ellipsoids is incomplete, as well. Many common order metrics are minimized for the, so-called, "maximally random jammed" (MRJ) packings [8]. Yet, it remains unclear, how the various protocols of compression, commonly starting from a fluidlike initial state, explore the available phase space and whether any fundamental physical reason exists for the convergence of many common compression protocols towards packings with densities close to that of the MRJ state [8–13].

In this work, we study the dependence of the bulk structure in fluids of ellipsoids on the aspect ratio $t = a/b$ of the constituent particles, where a and b are the polar and the equatorial diameters, respectively. We combine experiments, theory, and Monte Carlo (MC) simulations, to explore the fundamental role of the rotational degrees of freedom in these fluids, in the vicinity of the so-called "sphere point" ($t = 1$), where the coupling between rotations and translations vanishes. We demonstrate that the critical dependence of this coupling on $\epsilon \equiv |t - 1|$, for $\epsilon \to 0$, gives rise to a dramatic nondifferentiable variation of some structural and thermodynamic fluid properties. Strikingly, a similar nonanalytic behavior has been observed for the densities of jammed amorphous zero-temperature packings of frictionless ellipsoids [6,8,14], ellipses, and spherocylinders. Our observations suggest that vestiges of the jamming transition are present in thermodynamically equilibrated fluids, down to very low densities. We speculate that such vestiges may possibly be responsible for the jamming of many common fluid compression protocols near the so-called "random close packing" (rcp) of spheres, where particle volume fraction is ~0.64.

To resolve the local structure in fluids of ellipsoids, we employ ellipsoidal colloids, suspended in an organic solvent. Classical light, x-ray, or neutron scattering techniques, providing very precise structural information for spherically isotropic particles, do not allow the structure to be resolved in systems of ellipsoids; the separation between the form factor and the structure factor is a major challenge for moderate t, due to the coupling between particle positions and orientations [15,16]. To overcome this obstacle, we carry out real-space experiments, employing direct confocal microscopy [17]. We prepare our colloidal ellipsoids by a uniaxial stretching of PMMA (polymethymethacrylate) spheres [27–30], 2.4 ± 0.04 μm in diameter, as described elsewhere [4,5]. The particles are fluorescently labeled with Nile red for confocal microscopy and sterically stabilized by a poly-12-hydroxystearic acid (PHSA) monolayer [4,5,11]. We suspend the ellipsoids in a mixture of decahydronaphthalene and tetrachloroethylene (mass ratio of 1:1.1), where their rotational and positional

degrees of freedom are thermalized by the Brownian motion. This solvent mixture matches the density and the refractive index of the colloids, eliminating particle sedimentation and allowing confocal imaging deep into the bulk of the suspensions. The particle stretching procedure damages the PHSA monolayer [4,5,30]. For $t \lesssim 1.7$, the monolayer was replenished by readsorption of PHSA from a concentrated solution [30]. For higher aspect ratios, this procedure is insufficient and particle stabilization is achieved by introduction of the AOT (dioctyl sodium sulfosuccinate, Sigma-Aldrich 98%) micelles into the suspension. The AOT micelles charge the particles, but also screen long-range Coulomb repulsions [5,31], so that the interactions become quasihard at high AOT concentrations [32]. The coherent physical behavior observed in this work for the AOT- and the PHSA- stabilized particles, at different particle aspect ratios t and volume fractions ϕ, suggests that the chemical details of the stabilizing mechanism do not matter for our current purposes. In particular, as the AOT-stabilized colloids are prolate and almost spherical, they may be regarded as simple hard spheroids, the axes of which are slightly inflated beyond their geometrical size to account for the Coulomb charging [5,7].

As a quantitative characterization of the fluid structure, we obtain the radial distribution function $g(r)$ of the particle centers, resolved by the confocal microscopy [4,5]. $g(r)$ measures the probability for two particle centers within the fluid, to be separated by a distance r. In dense fluids, $g(r)$ exhibits oscillations, which correspond to the liquid coordination shells forming around each particle, several periods of such oscillations are clearly seen in Fig. 1. Note the excellent match between the experimental

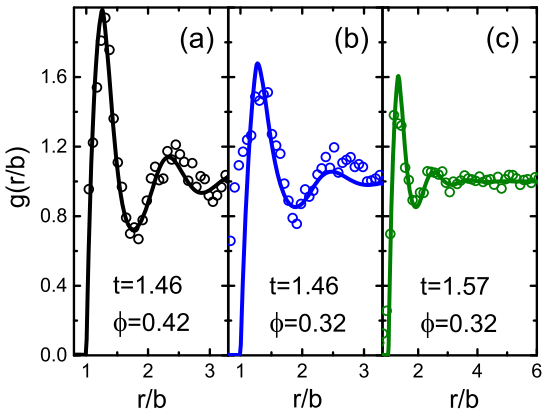

FIG. 1. Good agreement is observed between the PY-theoretical (solid curves) and the experimental (scatter) radial distribution functions $g(r)$. The data in sections (a), (b), and (c) are shown for several different particle aspect ratios t and volume fractions ϕ (see legend). The r values are normalized by the equatorial axis b of the ellipsoids. Note, the effective axes of the ellipsoids are slightly increased compared to the geometric ones, due to the charge effects (see text); the ϕ and t in the legends have been rescaled accordingly, to account for particle "inflation".

data (scatter) and the theoretical calculation (solid curves), which is based on the classical Percus-Yevick (PY) approximation [33]. This agreement has been achieved with only one adjustable parameter, which is the inflation of particle axes due to the Coulomb repulsions [5]. The amount of inflation was different for the AOT- and the PHSA-stabilized particles, yet stayed the same for different particle concentrations and aspect ratios. Importantly, once the amount of particle inflation is chosen, the volume fraction and the aspect ratio of the colloids are adjusted accordingly, with no additional free parameters, as detailed elsewhere [5]. A similar agreement with the experiment is achieved for the MC simulations of hard ellipsoids, which also perfectly match the PY data [17]. Interestingly, the $g(r)$ oscillations become less pronounced for larger t (Fig. 1), with the correlations in particle positions being lost in favor of the local orientational correlations.

To further explore the emergence of local orientational correlations, we study the $g(r)$ for a much denser set of t values near the sphere point. Clearly, the experimental studies become increasingly challenging for a vanishing ϵ. However, the observed agreement between MC simulations, PY theory, and experiments justifies our choice to explore the critical behavior at $\epsilon \to 0$ solely by means of theory and simulation.

The most prominent feature of the $g(r)$ is its principal peak position r_p. To explore the variation of r_p with the particle aspect ratio at a constant particle volume, we normalize r_p by $L \equiv (ab^2)^{1/3}$. Strikingly, r_p/L exhibits a nonanalytic behavior at the sphere point [scatter in Fig. 2(a)], where its derivative is discontinuous. This nonanalyticity is present for different ϕ and shows up for both PY- (solid symbols) and MC- (open symbols) derived values. Importantly, this cusplike feature at $t = 1$ is not an intrinsic geometrical property of an individual ellipsoid; for example, the radius of gyration of an individual ellipsoid is smooth for all t. Remarkably, the gull wing shape of r_p/L resembles the simulated variation, as a function of t, of the particle volume fraction ϕ_j in MRJ packings of the (nonfrictional) ellipsoids [6,8]. This resemblance is not just a coincidence. The most probable separation between adjacent particles r_p must be related to the free volume available for the particles in the fluid. The fraction of free volume in a fluid, measured with respect to the most disordered jammed state (the MRJ), is $\Delta\phi = 1 - \phi/\phi_j$. This $\Delta\phi$ has also a similar gull wing shape and a cusp at $t = 1$ [Fig. 2(b)], validating our choice of MRJ as a reference state for the free volume calculation. Indeed, the free volume calculated with respect to the densest crystalline packing of the ellipsoids [8] does not exhibit such a cusp and random sequential addition (RSA) of ellipsoids produces dilute packings [34], not allowing the fluid free volume to be measured with respect to RSA.

We justify the observed nonmonotonic variation of r_p/L in fluids by simple phenomenological arguments [17]. For

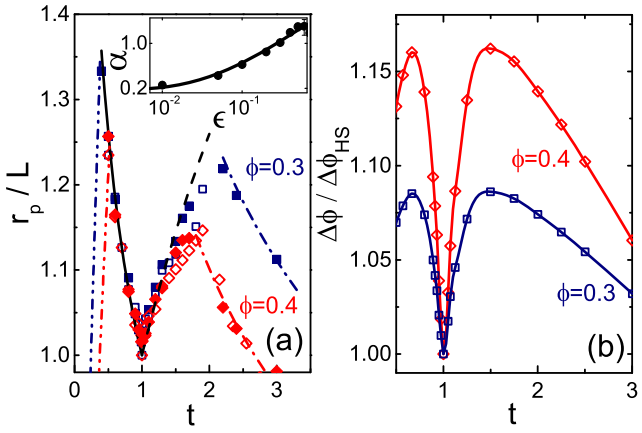

FIG. 2. (a) The separation between the nearest neighbors r_p is minimal for the spheres, with a gull wing shape exhibited as a function of t. The r_p values are normalized by $L = (ab^2)^{1/3}$, to keep the volume of the spheroids constant for all t. Data obtained by MC simulations (open symbols) and PY theory (solid symbols), for two different ϕ (see labels) stay in a very good agreement with our phenomenological predictions. Dashed and solid lines represent $r_p/L = t^{1/3}$ and $t^{-1/3}$, respectively, while dash-dotted and dash-double-dotted curves stay for $(0.77/\phi)^{1/2}t^{-1/3}$ and $(0.77/\phi)t^{2/3}$ (see text). The gull wing shape and the cusp at $t = 1$, exhibited by r_p/L, resemble the behavior of the free volume $\Delta\phi(t)$, shown in (b), where $\Delta\phi_{\rm HS} \equiv \Delta\phi(t = 1)$ is the free volume in a fluid of hard spheres at the same density. Averaging over all moderate-t data sets from section (a) minimizes the statistical noise; the resulting $\alpha \equiv r_p/L - 1$ (solid symbols in the inset, on a log-log scale) are perfectly matched [35] by $(\epsilon + 1)^{1/3} - 1 + \delta$ (solid curve), where $\delta = 0.0175$ is the accuracy of r_p/b determination.

large t, the orientational degrees of freedom dominate. While a true long-range nematic order is missing for these ϕ values, long particle axes are locally parallel. Thus, an ellipsoid of a geometric volume $\pi ab^2/6$ occupies, on average, a (roughly) ellipsoidal volume $\pi a r_p^2/6$ encompassing the particle [36]. Assuming that the volume fraction of the encompassing ellipsoids is $\sim$0.77, the densest packing in this range [8] of t, we obtain $r_p/L = (0.77/\phi)^{1/2}t^{-1/3}$, which perfectly matches our r_p/L, for both ϕ values (dash dotted lines in Fig. 2). A similar argument for the oblate particles at $t \ll 1$, where the volume of the encompassing ellipsoid is $\pi r_p b^2/6$, yields the dash-dot-dotted lines in Fig. 2(a). At the opposite limit $t \approx 1$, the orientations of nearly spherical particles are almost random, since the coupling between rotations and translations is very weak [37,38]. Therefore, the effective volume occupied by an oblate spheroid is a sphere of diameter b, which is the corresponding solid of revolution. In a fluid of such effective spheres, the first peak position [1,2] is $r_p = b$, so that $r_p/L = t^{-1/3}$. Once again, this prediction [solid line in Fig. 2(a)] perfectly matches our data. Finally, a short prolate spheroid, revolving freely about one of its equatorial axes, occupies an (oblate) spheroidal volume: $v_o = \pi a^2 b/6$. If such volumes are packed closely together, the separation between their centers scales as $\sim v_0^{1/3} \sim bt^{2/3}$. Identifying this separation with r_p, we obtain $r_p/L \sim t^{1/3}$. Recalling that $r_p/L = 1$ for the spheres, we obtain $r_p/L = t^{1/3}$. This relation is shown by dashes in Fig. 2(a), in a perfect agreement with both PY- and MC-generated data. Furthermore, we average the PY- and MC-r_p/L values for both ϕ in Fig. 2(a), demonstrating a perfect agreement with the proposed phenomenological expressions for oblate and prolate particles [35] of moderate t [inset to Fig. 2(a)]; for this agreement to be achieved, the average resolution of our r_p/L values $\delta = 0.0175$ had to be taken into account, dictated by the r/b-step size of the PY- and MC- $g(r)$ data being 0.015 and 0.02, respectively. Remarkably, our phenomenological arguments demonstrate that in contrast with the packings of pennies or pancakes, oblate spheroids do not tend, at moderate t, to orient in parallel to each other. Similarly, the prolate spheroids exhibit a significant freedom of rotation for $t \lesssim 2$. Thus, in contrast with the common intuition, the nonanalytic behavior at $t = 1$ is not caused by a different mutual orientation of the adjacent particles for $t \to 1^+$ and $t \to 1^-$. Moreover, the fact that our phenomenological arguments reproduce the behavior of r_p/L in fluids, and the similar shape of r_p/L and $\Delta\phi$ (Fig. 2), suggest that analogous arguments may possibly be employed to describe the local microscopic structure in jammed granular packings.

To explore the role of particle anisotropy for the fluid structure beyond the first coordination shell, we use the $g(r)$ to define a positional order parameter [39]: $\tau \equiv \int_0^\infty |g(r) - 1|^2 r^2 dr$, where r is in units of L. By definition, $\tau = 0$ for an ideal gas, where all correlations are missing. At a given ϕ, the strongest positional correlations occur for the spheres, where the orientations are completely disordered [see Fig. 3(a)]. The coupling to rotations increases for larger ϵ, resulting into a dramatic *decrease* of positional correlations measured by τ. Strikingly, τ exhibits a nonanalytic behavior at $t = 1$, as clearly demonstrated by both the PY and the MC methods. Remarkably, while the PY approach employs the classical Berne and Pechukas approximation to calculate the pair potentials [33], no such approximation is used in the MC simulations; thus, the agreement between the PY theory and the simulations strongly supports the validity of our results. Also, the experimental τ (solid symbols) match correctly the theoretical trends. As expected, for moderate t, τ increases with the particle volume fraction. In particular, for the spheres, $\tau_{\rm HS} \equiv \tau(1)$ diverges as $(0.64 - \phi)^{-1.75\pm.08}$ [Fig. 3(b)]. The divergence of τ, obtained for the equilibrium fluids, complements the previously reported [9] divergence of the *metastable* fluid equation of state at $\phi = 0.64$, which has been highly controversial [13] because of the ambiguity of the metastable fluid branch. The observed behavior suggests that a

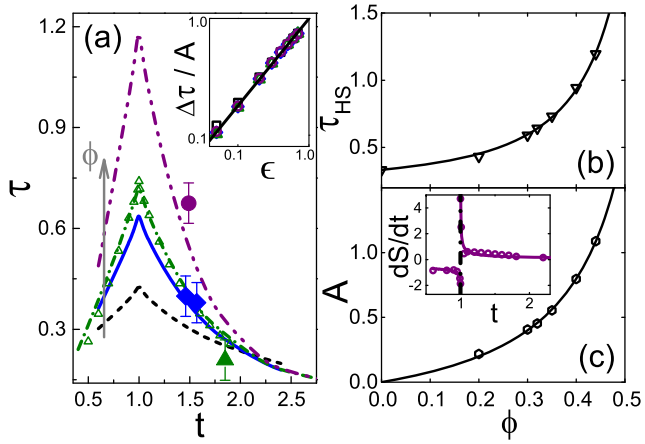

FIG. 3. (a) The strength of short-range positional correlations τ is a nonanalytic function of the particle aspect ratio t. The data are shown for $\phi = 0.20, 0.32, 0.35, 0.44$ (from bottom to top, see ϕ arrow), where rhombi, triangles, and circles correspond to $\phi = 0.32$, 0.35, and 0.44, respectively. A very good agreement is shown for the PY theory (lines), the MC simulations (open triangles), and the experiment (solid symbols); note, the experimental symbols have been shifted by a factor of 1.5, to compensate for possible inaccuracies of particle tracking. The inset demonstrates a collapse of τ for all ϕ; the corresponding normalization factors $A(\phi)$ are shown in (c). $\Delta\tau$ is the (absolute value of the) excess τ, compared to that of the hard spheres (τ_{HS}) at the same ϕ; the latter is shown in (b) to diverge towards $\phi \approx 0.64$. The inset in (c) demonstrates a discontinuity at $t = 1$ in the derivative dS/dt of the excess translational entropy, as in a second-order phase transition; here dS/dt is obtained for $\phi = 0.44$ and normalized by $-2\pi k_B \rho L^3$ for nondimensionalization.

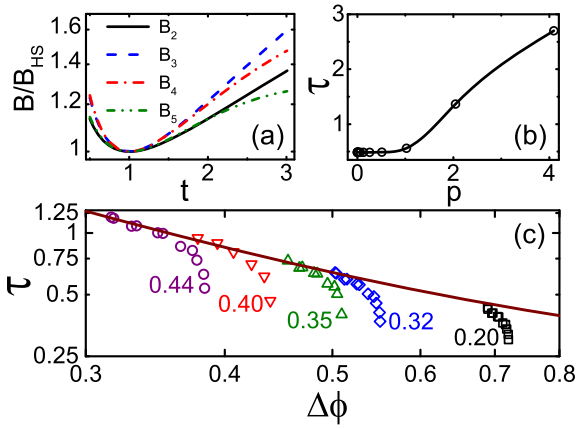

FIG. 4. (a) The second–fifth virial coefficients of the ellipsoids [42] (see legend) exhibit a smooth variation with t near the sphere point, indicating that the nonanalytic behavior of $\tau(t)$ and $S(t)$ is caused by higher-order terms of the virial expansion, as in the critical phenomena. (b) Not all types of spherical anisotropy are the same. In fluids of dipolar spheres [17], interacting through a truncated Lennard-Jones potential [5], τ is a smooth function of the dipole magnitude p, down to $p = 0$, where rotational anisotropy completely vanishes; p is in the Lennard-Jones units [17]. (c) The magnitude of translational correlations τ in fluids of ellipsoids is fully determined, for small ϵ, by the free volume in the fluid, with respect to the MRJ packing of the corresponding ellipsoids. For larger ϵ, nonuniversal deviations from this scaling (solid curve) are observed. Labels indicate the ϕ value of each data set; the data were obtained by PY calculations.

deep relation exists between the local structure in fluids and the onset of jamming, where a global percolating force network forms [10,13].

The observed nonanalyticity of τ and r_p at $t = 1$ suggests that some other properties of the fluid may also be singular at the sphere point, as in the case of a phase transition. To directly test the fluid thermodynamics, we calculate the excess translational entropy (relative to an ideal gas at the same density), approximated [40,41] by: $S \approx -2\pi k_B \rho \int [g(r)\ln g(r) - g(r) + 1] r^2 dr$, where k_B is the Boltzmann factor and ρ is the particle number density. As expected, the derivative dS/dt is discontinuous at the sphere point [inset to Fig. 3(c)], reminiscent of a second-order transition. Furthermore, we observe that the critical scaling of $\Delta\tau \equiv |\tau(t) - \tau_{\mathrm{HS}}|$ allows the $\Delta\tau$ for all ϕ to be collapsed together [inset to Fig. 3(a)], indicating that $\Delta\tau = A(\phi)\epsilon^{3/4}$; here $A(\phi)$ is a function of ϕ only, diverging as $|\phi - 0.64|^{-1.24\pm.04}$ [Fig. 3(c)]. The observed divergence of $A(\phi)$ is caused by the divergence of $\tau_{\mathrm{HS}}(\phi)$ and does not necessarily imply a divergence of $\tau(t > 1)$. Indeed, studies of granular packings of ellipsoids [6,8], demonstrate that the jamming in these systems occurs at a higher ϕ.

The nondifferentiability of τ at $t = 1$, precluding series expansion, demonstrates that the rotational anisotropy, missing for the simple spheres, qualitatively changes the fluid structure. Interestingly, the virial coefficients of the ellipsoids [42], in contrast with $\tau(t)$, exhibit a smooth variation in the vicinity of the sphere point [Fig. 4(a)], indicating that the nonanalyticity of τ is caused by a complex collective behavior in the fluid, rather than being a trivial property of the particle geometry. Moreover, we observe a continuous variation of τ in molecular dynamics simulations of a dipolar fluid [17], as the magnitude of the dipole is taken continuously to zero [Fig. 4(b)]. Thus, the emergence of different types of spherical anisotropy influences the fluid structure in a different manner.

Finally, it is highly appealing to regard a fluid of ellipsoids as simply an expanded jammed packing. In such case, the only relevant parameter is $\Delta\phi$. Our τ values, plotted for all different ϕ and t as a function of $\Delta\phi$ [Fig. 4(c)] demonstrate that a common scaling (solid curve) can be found, matching all data at small ϵ. However, for larger ϵ, the data significantly deviate from the common curve, indicating that $\Delta\phi$ is no longer the only important parameter; other related manifestations of nonuniversality have been recently detected [43]. This behavior is reminiscent of a critical scaling near the classical phase transitions, where a universal behavior applies at the critical point, yet deviations may be observed when the system is further away from the criticality.

In conclusion, we demonstrate that a nonanalytic behavior of structural and thermodynamic fluid properties occurs at the sphere point, reminiscent of a second-order phase transition. We relate this transition to the emergence of a coupling between translations and rotations at $t = 1$, which is also responsible for similar nonanalyticities in structural properties of jammed granular packings of ellipsoids [6,8,14], ellipses [44], and spherocylinders [45]. Moreover, fingerprints of such nonanalyticities seem also to show up in critical temperatures and concentrations of liquid-vapour transitions in attractive liquids [46], emphasizing the importance of the simpler athermal systems studied in our present work. We describe some aspects of the observed liquid-liquid transition by phenomenological free volume arguments, suggesting that the MRJ packing of ellipsoids plays a role of a ground state for these fluids. Future theoretical and experimental research, directly probing the orientational degrees of freedom in these systems, should provide a deeper insight onto the physics of fluids and random granular packings, providing a better understanding of the ground states of matter.

E. S and A. P. C thank the Israel Science Foundation (Grants No. 85/10, No. 1668/10) for financial support. Some of the equipment was funded by the Kahn foundation. E. S thanks S. Rubinstein, W. Kob, D. C. Rapaport, A. V. Butenko, and S. Torquato for fruitful discussions. D. Friedman, A. V. Butenko, and M. Schultz are acknowledged for technical assistance.

*eli.sloutskin@biu.ac.il

[1] R. P. A. Dullens, D. G. A. L. Aarts, and W. K. Kegel, Proc. Natl. Acad. Sci. U.S.A. **103**, 529 (2006).
[2] P. J. Lu, F. Giavazzi, T. E. Angelini, E. Zaccarelli, F. Jargstorff, A. B. Schofield, J. N. Wilking, M. B. Romanowsky, D. A. Weitz, and R. Cerbino, Phys. Rev. Lett. **108**, 218103 (2012).
[3] L. C. Hsiao, B. A. Schultz, J. Glaser, M. Engel, M. E. Szakasits, S. C. Glotzer, and M. J. Solomon, Nat. Commun. **6**, 8507 (2015).
[4] A. P. Cohen, E. Janai, E. Mogilko, A. B. Schofield, and E. Sloutskin, Phys. Rev. Lett. **107**, 238301 (2011).
[5] A. P. Cohen, E. Janai, D. C. Rapaport, A. B. Schofield, and E. Sloutskin, J. Chem. Phys. **137**, 184505 (2012).
[6] A. Donev, I. Cisse, D. Sachs, E. A. Variano, F. H. Stillinger, R. Connelly, S. Torquato, and P. M. Chaikin, Science **303**, 990 (2004).
[7] S. Dorosz, N. Shegokar, T. Schilling, and M. Oettel, Soft Matter **10**, 4717 (2014).
[8] S. Torquato and F. H. Stillinger, Rev. Mod. Phys. **82**, 2633 (2010).
[9] R. D. Kamien and A. J. Liu, Phys. Rev. Lett. **99**, 155501 (2007).
[10] A. J. Liu and S. R. Nagel, Annu. Rev. Condens. Matter Phys. **1**, 347 (2010).
[11] S. R. Liber, S. Borohovich, A. V. Butenko, A. B. Schofield, and E. Sloutskin, Proc. Natl. Acad. Sci. U.S.A. **110**, 5769 (2013).
[12] Z. Zhang, N. Xu, D. T. N. Chen, P. Yunker, A. M. Alsayed, K. B. Aptowicz, P. Habdas, A. J. Liu, S. R. Nagel, and A. G. Yodh, Nature (London) **459**, 230 (2009).
[13] G. Parisi and F. Zamponi, Rev. Mod. Phys. **82**, 789 (2010).
[14] A. Baule, R. Mari, L. Bo, L. Portal, and H. A. Makse, Nat. Commun. **4**, 2194 (2013).
[15] E. B. Mock and C. F. Zukoski, Langmuir **23**, 8760 (2007).
[16] M. Reufer, V. A. Martinez, P. Schurtenberger, and W. C. K. Poon, Langmuir **28**, 4618 (2012).
[17] See Supplemental Material at http://link.aps.org/supplemental/10.1103/PhysRevLett.116.098001, which includes Refs. [18–26], for a detailed description of sample preparation and imaging procedures. Computer simulations are described and compared to the theory. A detailed explanation of the phenomenological arguments, used to reproduce the data in Fig. 2(a), is provided as well.
[18] G. Bryant, S. R. Williams, L. Qian, I. K. Snook, E. Perez, and F. Pincet, Phys. Rev. E **66**, 060501(R) (2002).
[19] P. J. Lu, P. A. Sims, H. Oki, J. B. Macarthur, and D. A. Weitz, Opt. Express **15**, 8702 (2007).
[20] P. J. Lu, M. Shutman, E. Sloutskin, and A. V. Butenko, Opt. Express **21**, 30755 (2013).
[21] J. C. Crocker and D. G. Grier, J. Colloid Interface Sci. **179**, 298 (1996).
[22] B. D. Leahy, X. Cheng, D. C. Ong, C. Liddell-Watson, and I. Cohen, Phys. Rev. Lett. **110**, 228301 (2013).
[23] C. B. Barber, D. P. Dobkin, and H. T. Huhdanpaa, ACM Trans. Math. Softw. **22**, 469 (1996).
[24] W. C. K. Poon, E. R. Weeks, and C. P. Royall, Soft Matter **8**, 21 (2012).
[25] C. De Michele, A. Scala, R. Schilling, and F. Sciortino, J. Chem. Phys. **124**, 104509 (2006).
[26] S. Plimpton, J. Comp. Physiol. **117**, 1 (1995); http://lammps.sandia.gov.
[27] A. Mohraz and M. J. Solomon, Langmuir **21**, 5298 (2005).
[28] D. Florea and H. M. Wyss, J. Colloid Interface Sci. **416**, 30 (2014).
[29] C. C. Ho, A. Keller, J. A. Odell, and R. H. Ottewill, Colloid Polym. Sci. **271**, 469 (1993).
[30] Z. Zhang, P. Pfleiderer, A. Schofield, C. Clasen, and J. Vermant, J. Am. Chem. Soc. **133**, 389 (2011).
[31] G. S. Roberts, R. Sanchez, R. Kemp, T. Wood, and P. Bartlett, Langmuir **24**, 6530 (2008).
[32] T. Kanai, N. Boon, P. J. Lu, E. Sloutskin, A. B. Schofield, F. Smallenburg, R. van Roij, M. Dijkstra, and D. A. Weitz, Phys. Rev. E **91**, 030301R (2015).
[33] M. Letz and A. Latz, Phys. Rev. E **60**, 5865 (1999).
[34] J. D. Sherwood, J. Phys. A **30**, L839 (1997).
[35] Note, the $\alpha(\epsilon)$ dependence is the same for $t > 1$ and $t < 1$ in the limit of $\epsilon \to 0$, as $(1+\epsilon)^{1/3}/(1-\epsilon)^{-1/3} = 1 + O(\epsilon^2)$. Separating the $t > 1$ and $t < 1$ values in the inset to Fig. 2(a) allows the same quality of a fit to be obtained, yet with the statistical spread of data being larger.

[36] C. Baravian, L. J. Michot, E. Paineau, I. Bihannic, P. Davidson, M. Impéror-Clerc, E. Belamie, and P. Levitz, Europhys. Lett. **90**, 36005 (2010).
[37] Z. Zeravcic, N. Xu, A. J. Liu, S. R. Nagel, and W. van Saarloos, Europhys. Lett. **87**, 26001 (2009).
[38] M. Mailman, C. F. Schreck, C. S. O'Hern, and B. Chakraborty, Phys. Rev. Lett. **102**, 255501 (2009).
[39] S. Torquato, G. Zhang, and F. H. Stillinger, Phys. Rev. X **5**, 021020 (2015).
[40] T. M. Truskett, S. Torquato, and P. G. Debenedetti, Phys. Rev. E **62**, 993 (2000).
[41] Z. Zheng, R. Ni, F. Wang, M. Dijkstra, Y. Wang, and Y. Han, Nat. Commun. **5**, 3829 (2014).
[42] C. McBride and E. Lomba, Fluid Phase Equilib. **255**, 37 (2007).
[43] F. M. Schaller, S. C. Kapfer, J. E. Hilton, P. W. Cleary, K. Mecke, C. De Michele, T. Schilling, M. Saadatfar, M. Schröter, G. W. Delaney, and G. E. Schröder-Turk, Europhys. Lett. **111**, 24002 (2015).
[44] C. F. Schreck, N. Xu, and C. S. O'Hern, Soft Matter **6**, 2960 (2010).
[45] S. R. Williams and A. P. Philipse, Phys. Rev. E **67**, 051301 (2003).
[46] S. Varga, E. Meneses-Juárez, and G. Odriozola, Soft Matter **9**, 11178 (2013).

Structural transition in a fluid of spheroids: a low-density vestige of jamming Supplementary Information

A. P. Cohen,[1] S. Dorosz,[2] A. B. Schofield,[3] T. Schilling,[2] and E. Sloutskin[1]

[1] *Physics Department and Institute of Nanotechnology & Advanced Materials, Bar-Ilan University, Ramat-Gan 5290002, Israel*
[2] *Research Unit for Physics and Materials Science, Université du Luxembourg, L-1511 Luxembourg, Luxembourg*
[3] *The School of Physics and Astronomy, University of Edinburgh, Edinburgh EH9 3JZ UK*

(Dated: February 7, 2016)

PREPARATION AND CHARACTERIZATION OF PROLATE COLLOIDAL SPHEROIDS

To prepare prolate ellipsoidal colloids, we uniaxially stretch simple colloidal spheres, following the procedure[4,5,18,21] which was used in the past with polystyrene[20] and poly(methylmethacrylate) (PMMA) particles stabilized by a grafted layer of PMMA-g-PDMS [poly(dimethylsiloxane)] copolymer. Our initial spherical colloids are made of PMMA and coated by a sterically-stabilizing layer of polyhydroxystearic acid (PHSA). The thickness of the PHSA monolayer[38] is $\sim$ 10 nm, such that the interparticle potential between the initial colloids is closely approximated by the hard sphere model. The reason for choosing PMMA, rather than polystyrene or inorganic materials, is that the density and the refractive index of PMMA can be matched by mixtures of common organic solvents to form stable suspensions, where light scattering is minimized for confocal imaging deep into the bulk of the sample. The initial spheres are fluorescently labeled by the Nile Red dye, for confocal measurements. The diameter of the initial spheres is $\sigma_s = 2.4$ μm, as determined by static and dynamic light scattering. The polydispersity of the initial spheres is below 4%, measured by scanning electron microscopy (SEM). To characterize the size and the shape of the particles[5], we deposit them from hexane onto a clean aluminum substrate. SEM images are then obtained at 30 keV, employing the Quanta Inspect (FEI^{TM}) setup.

For the stretching of the colloidal spheres[4,5,18,21], we suspend these spheres in a 25% (w/w) solution of hydroxy terminated PDMS (typical molecular weight $M_n = 10^5$, Sigma-Aldrich) in hexane (BioLab, AR $>$ 96%). The volume fraction of spheres in this mixture is low, $\phi \approx 0.03$. Next, a cross-linking agent, trimethylsilyl terminated poly(dimethylsiloxane-co-methylhydrosiloxane) ($M_n = 950$, Sigma-Aldrich) and a catalyst [tin(II) 2-ethylhexanoate, Sigma-Aldrich, $\sim$ 95%] are added to polymerize the PDMS. The weight fractions of the cross-linking agent and the catalyst are 6×10^3 and 8×10^3, respectively. Immediately after the introduction of the cross-linking agent and the catalyst, the suspension is poured onto a rectangular mold, so that a $\sim$ 1mm-thick composite rubber film forms in the mold. To avoid trapping of small air volumes in the rubber, the procedure is carried out in vacuum[19], at $\sim$ 1 mTorr. After a curing time of $\sim$ 13 hrs, the films are post-cured for 2 hrs in an oven, pre-heated to 120° C. The rubber is then uniaxially stretched to a desired length inside an oven, at $T = 165°$ C, above the glass transition temperature of PMMA. For the stretching process to be accurate and reproducible, for minimization of film tearing, and in order to reduce the shape polydispersity of the resulting ellipsoids, we have constructed a computerized stretching device. This device, mounted inside an oven, is capable of stretching the films at sufficiently slow and uniform rates, $<$ 70 μm/s. The door of our oven is equipped by a glass window, allowing the stretching process to be followed visually in real time.

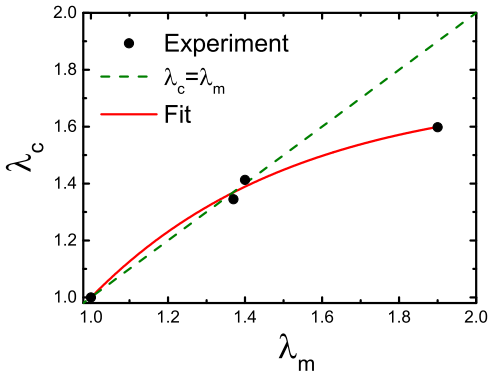

FIG. 1. The extension ratio of the PMMA colloids λ_c (scatter), is shown as a function of the extension ratio of the composite PDMS matrix λ_m. The non-linear behavior of $\lambda_c(\lambda_m)$ indicates that increasingly large strains of PDMS are needed to stretch the colloids to a high aspect ratio. Thus, the brittleness of the PDMS matrix limits the achievable t values of the colloids. Green dashes correspond to a perfect match between the strains of PDMS and PMMA, $\lambda_c = \lambda_m$. A phenomenological fit (see text) is shown in a red line.

Assuming that the volume of an individual particle is conserved in the stretching process, the aspect ratio t of the particle is a function of the elongation $\delta\sigma$ of its diameter: $t = (1 + \delta\sigma/\sigma_s)^{3/2}$. Thus, the extent of stretching of the PDMS matrix, with the spheres in it, determines the aspect ratio of the ellipsoids. Importantly, the extension ratio of the PMMA colloids $\lambda_c = (\sigma_s + \delta\sigma)/\sigma_s$

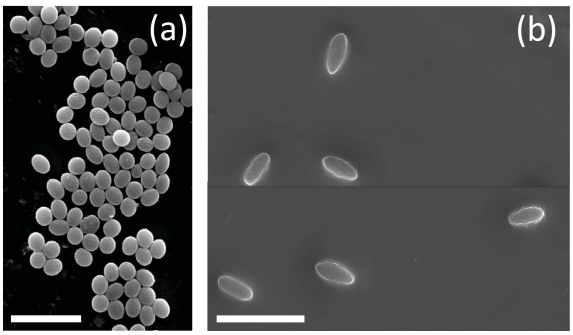

FIG. 2. SEM images of prolate colloidal ellipsoids, for the PDMS matrix stretched to an extension ratio of (a) $\lambda_m = 1.4$, (b) $\lambda_m = 1.9$. Note, the particles in panel (a) are oriented at different angles to the substrate, so that the apparent aspect ratios are smaller than the actual ones. Panel (b) was obtained by stitching of two separate SEM images, as marked by the horizontal black line.

is in general deviating from that of the PDMS matrix, $\lambda_m = (l + \delta l)/l$; here l is the initial length of the matrix, stretched to a length of $(l+\delta l)$. The experimental $\lambda_c(\lambda_m)$ relation is shown in Fig. 1 (black symbols), exhibiting a significant deviation from the naïve $\lambda_c = \lambda_m$ (green dashes). We can fit the experimental data by a phenomenological expression $\lambda_c = 1.73 - 4.89\exp(-\lambda_m/0.53)$ (red line in Fig. 1). The observed $\lambda_c(\lambda_m)$ indicates that for large extension ratios, the strain of PMMA colloids is much smaller than that of the composite PDMS matrix, as if the PMMA exhibits a strain stiffening response.

Two typical SEM images of the ellipsoids, as obtained by the described stretching procedure, are shown in Fig. 2. Similar SEM images are employed to measure the distribution $P(t)$ of the aspect ratios of the colloids. Particle inclination angles, with respect to the (roughly) horizontal substrate, make them appear shorter in SEM images[5]. Fortunately, the volumes of our ellipsoids, obtained by volume-conserving stretching of monodisperse spheres, are almost perfectly monodisperse. Moreover, our particles are prolate spheroids; as such, they are symmetric under rotation about their long axis. Therefore, the minor axis of a particle b can be measured quite accurately by SEM, being independent of the inclination angle of the particle with respect to the substrate. We obtain the aspect ratio and the inclination angle of each individual particle in our SEM images, based on the known volume of the initial spheres ($v = 7.24\ \mu m^3$) and the minor axis length b of the given particle, measured by SEM: $t = 6v\pi^{-1}b^{-3}$. The distribution $P(b)$, based on ~ 100 SEM images of colloidal particles, is shown in solid symbols in Fig. 3 for two different λ_c values. The peak position of the Gaussian fit (not shown) to the symmetric part of these $P(b)$ yields $t = 1.68 \pm 0.06$ for Fig. 2(a) and Fig. 3(a); $t = 2.02 \pm 0.06$ is obtained for Fig. 2(b) and Fig. 3(b).

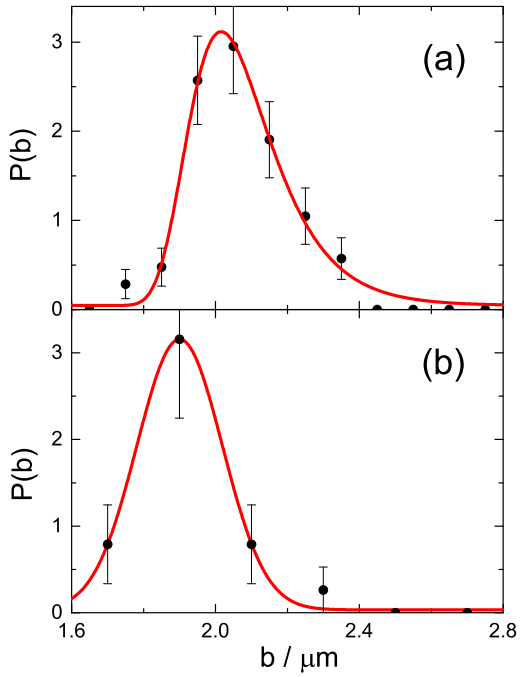

FIG. 3. Distributions of the minor axes lengths b of colloidal ellipsoids, as obtained by SEM for: (a) $\lambda_m = 1.4$, (b) $\lambda_m = 1.9$, corresponding to Fig. 2(a) and Fig. 2(b), respectively. The distribution peaks at $b = 2.02$ μm for (a) and at $b = 1.9$ μm for (b), corresponding to $t = 1.68 \pm 0.02$ and $t = 2.02 \pm 0.02$, respectively. The solid curves are fits by the Gumbel probability density function.

PARTICLE LOCATION ALGORITHM

Our algorithm for the detection of particle center positions and orientational angles is based on the PLuTARC algorithm, as also on the well-known algorithm of Crocker and Grier[41], previously used for tracking of colloidal spheres[39-40]. The algorithm, implemented in C/C++, takes as an input a three-dimensional stack of confocal slice images through the sample. The output consists of a list of (x,y,z) particle center coordinates and orientational angles.

The algorithm includes three stages. In the first stage, each individual two-dimensional (2D) confocal slice is analyzed. The slice is processed, so that the fluorescent colloids appear as bright, well-separated features on a dark background. A two-dimensional slice through an ellipsoidal particle is an ellipse. The center positions and the orientational angles of all such ellipses, in each of the two-dimensional slices, are measured. To find the orientational angles, we calculate the covariance matrix of the fluorescent intensity distribution at each of the particle

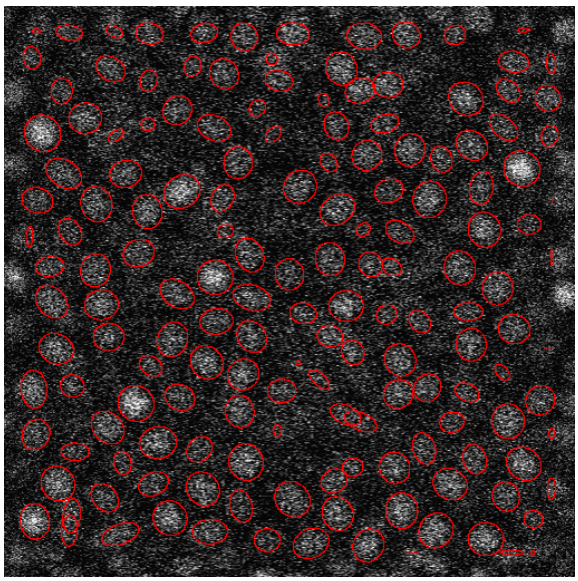

FIG. 4. A raw confocal image (2D slice, 42.4×42.4 μm^2) through a suspension of ellipsoids ($t = 1.68$, $\phi = 0.21$). The positions and the orientations of the particles, as detected by the first stage of our algorithm are marked by red ellipses. Note, all particles which are not perfectly parallel to the optical slice appear more rounded than they actually really are. Particles located next to the edges are excluded from the analysis, to avoid biasing of their centers by edge effects.

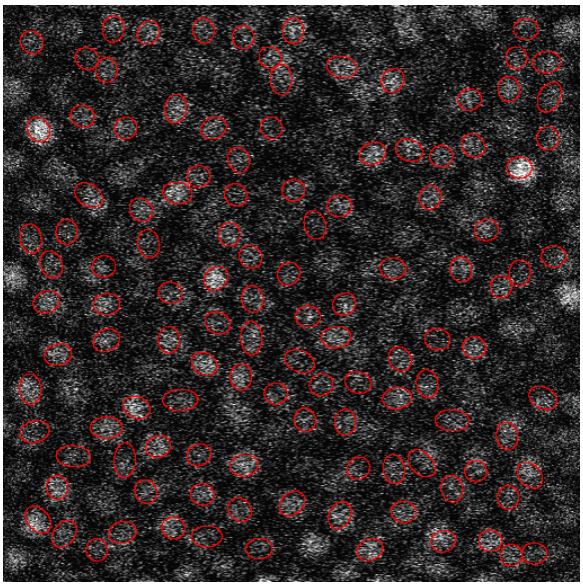

FIG. 5. A raw confocal image (2D slice, 42.4×42.4 μm^2) through a suspension of ellipsoids ($t = 1.68$, $\phi = 0.21$). The ellipses calculated by our algorithm from the full (3-stage) 3D reconstruction of the sample are marked in red ellipses. Note, some particles located outside of the focal plane are still visible in the image; those particles are dimmer than the rest and do not appear in the reconstruction. Particles located next to the edges are excluded, as in Fig. 4.

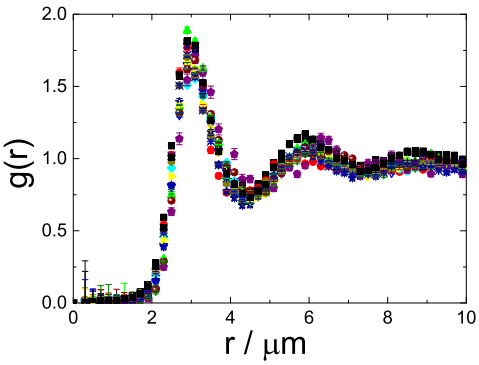

FIG. 6. The radial distribution functions (RDF) obtained from 2D slices, at different positions within the sample (different symbols), perfectly overlap. Here the aspect ratio and the volume fraction of the particles are $t = 1.68$ and $\phi = 0.21$, respectively.

positions. By diagonalization of the covariance matrices, the orientations of all elliptical slices through each of the colloids are obtained. The success of this procedure is demonstrated in Fig. 4, where the detected particle positions and orientations (red ellipses) are overlayed on top of the raw confocal slice image, for visual examination. The second stage of the algorithm links between centers of ellipses belonging to different slices, based on the lateral distance between their (x, y) coordinates and on the orientation of the ellipses. The third stage finds the direction of each ellipsoid in three dimensions. For that purpose, for each ellipsoid we retrieve from all the relevant confocal slices the three dimensional (3D) matrix of fluorescence intensity $I(x, y, z)$. The corresponding covariance matrix is then diagonalized, yielding the 3D orientation of the ellipsoid[42].

We visually examine the detected positions and orientations. For that, our codes use the reconstructed coordinates (x, y, z) and orientations (θ, ϕ) of the particles to calculate the appearance of (an elliptical cut through) each particle in each of the confocal slices. These calculated ellipses are overlayed on top of the raw confocal images, allowing the quality of the full 3D reconstruction to be assessed by visual examination (see Fig. 5).

We use the detected particle positions (x, y) in each slice (obtained in the first stage of the algorithm) to compute the radial distribution function (RDF). The RDF is then averaged over all slices to improve the statistics. The RDFs obtained at different positions within the sample perfectly overlap, as demonstrated by solid symbols in Fig. 6. The full 3D particle positions (x, y, z), obtained in the second stage of the algorithm, yield similar $g(r)$ as well.

To determine the local volume available for each individual particle, we carry out the Voronoi tessellation of our sample, employing the Qhull software[43]. To es-

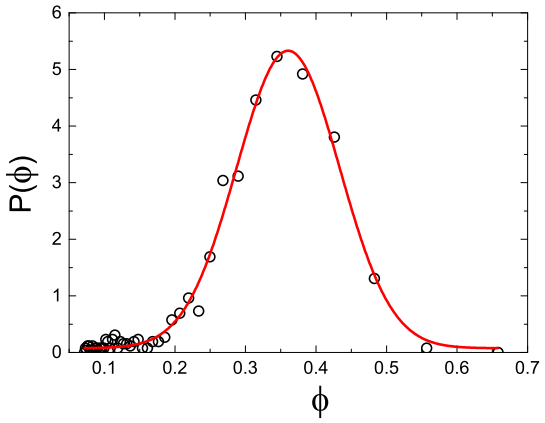

FIG. 7. A typical distribution of local volume fractions ϕ in a fluid of colloidal ellipsoids.

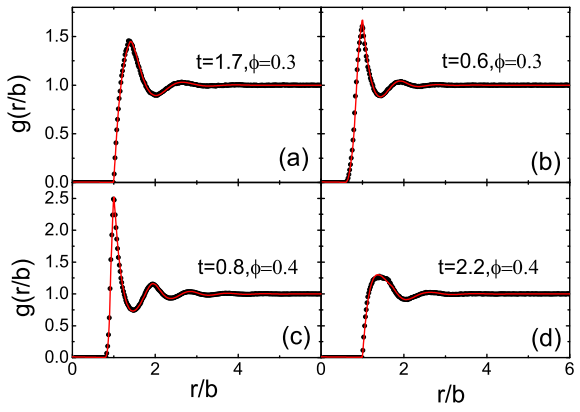

FIG. 8. The radial distribution functions of fluids of hard spheroids, obtained by Monte Carlo simulations (symbols) are perfectly matched by the PY-theoretical calculations (solid curves). The data are shown for different volume fractions ϕ and aspect ratios t (see labels), both for the oblate and the prolate particles. The r values are normalized by the equatorial axis of the ellipsoids b.

timate the local volume fraction ϕ in a suspension of prolate colloidal ellipsoids, we divide the single-particle volume $v = \pi t b^3/6$ by the volume V_V of the corresponding Voronoi cell, $\phi = v/V_V$ (see Fig. 7). $P(\phi)$ peak position provides an accurate estimate for the actual ϕ in the suspension[44].

COMPUTER SIMULATIONS

Fluids of hard ellipsoids

Monte Carlo simulations of hard ellipsoids were carried out at fixed particle number $N = 17496$, volume V and temperature T. The trial moves consisted of particle translations and rotations with a maximal distance of $1.210^{-3}b$ for the translation move and a maximal rotation by 0.42^0. We sampled all data over several self diffusion times $\tilde{\tau}$ (3-5 $\tilde{\tau}$ for the higher packing fractions and up to 20 $\tilde{\tau}$ for the lower packing fractions); here $\tilde{\tau}$ is the translational long-time self-diffusion time, i.e. the time an ellipsoid needs to diffuse over the length of its equatorial diameter. The simulated $g(r)$ are in a perfect agreement with the ones obtained numerically, employing the approximate Percus-Yevick (PY) closure to solve the Ornstein-Zernike equation for hard ellipsoids[24] (see Fig. 8). Our PY-generated structure factors are also in an excellent agreement with the molecular dynamics simulations[45].

Fluids of soft dipolar particles

Molecular dynamics (MD) simulations of dipole-bearing particles [Fig. 4(b) of the main text] were carried out employing LAMMPS[46]. In addition to the dipole-dipole interactions u_{pp}, the particles interact via a repulsive truncated Lennard-Jones (Weeks-Chandler-Andersen) potential:

$$u_{LJ}(r) = \begin{cases} 4\epsilon[(\sigma/r)^{12} - (\sigma/r)^6 + 1/4] & r < r_c = 2^{1/6}\sigma \\ 0 & r \geq r_c \end{cases} \quad (1)$$

The parameters σ and ϵ can be used to define convenient MD length and energy units, respectively, with mass expressed in terms of the sphere mass, and the MD temperature unit T obtained by setting $k_B = 1$. The dipole-dipole interaction is given by: $u_{pp} = r^{-3}\overrightarrow{p_i}\cdot\overrightarrow{p_j} - 3r^{-5}(\overrightarrow{p_i}\cdot\overrightarrow{r})(\overrightarrow{p_j}\cdot\overrightarrow{r})$, where $\overrightarrow{p_i}$ and $\overrightarrow{p_j}$ are the dipole moments of the i-th and the j-th particles, respectively; u_{pp} is cut off at $r = 3\sigma$. The simulations involve systems of 1000 particles, running at $T = 0.33$. Periodic boundaries are used in all three dimensions and the simulation cell size is determined by the overall number density, $\rho^\star = 0.4$, in Lennard-Jones units.

SCALING OF r_p/L: PHENOMENOLOGICAL ARGUMENTS

In the main text, the non-monotonic variation of r_p/L with the aspect ratio is explained by phenomenological arguments, which single out four possible regimes: (a) $t \gg 1$; (b) $t \ll 1$;(c) $t \leq 1$; (d) $t \geq 1$. These four regimes are schematically depicted in Fig. 9, where the particles are yellow and their effective occupied volume is denoted by black ellipses and circles.

In Fig. 9(a-b), the particles have their long axes

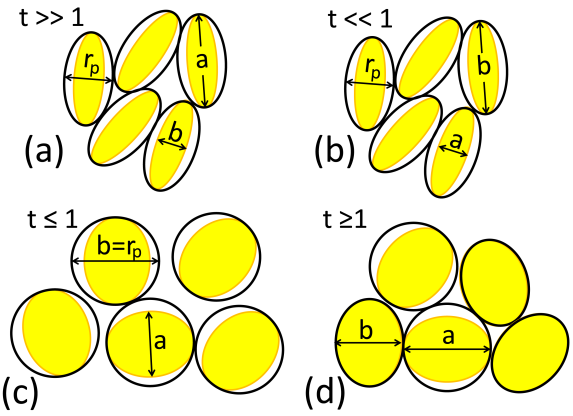

FIG. 9. Schematic representation of four different regimes of packing in fluids of spheroids: (a) $t \gg 1$; (b) $t \ll 1$;(c) $t \leq 1$; (4) $t \geq 1$. Particle cross-sections are shown in yellow; the excluded volumes are depicted as black ellipses and circles. r_p is the position of the principal peak of the $g(r)$; a is the symmetry axis.

aligned, locally, in parallel. Importantly, while for the prolate particles [Fig. 9(a)] the long axis is the polar one, for the oblate ones [Fig. 9(b)] the equatorial axes are the longer ones. The densest packing[6] of the effective volumes in Fig. 9(a-b), at a volume fraction of ~ 0.77, yields $r_p = (0.77/\phi)^{1/2}b$ for the prolate particles and $r_p = (0.77/\phi)a = (0.77/\phi)bt$ for the oblate ones. Here $\phi = N\pi tb^3/6/V$ is the volume fraction of N colloidal spheroids in volume V; the expressions for r_p result by noting that the number density of particles N/V is equal to that of their excluded volumes, while the volume fractions are ϕ and 0.77, respectively. The obtained r_p are then divided by $L = bt^{1/3}$, to obtain the dash-dotted and dash-double-dotted lines in Fig. 2(a) of the main text.

The other two regimes, corresponding to almost-spherical oblate and prolate particles, are shown in Fig. 9(c) and Fig. 9(d), respectively. In these regimes the particles rotate freely. Thus, the excluded volumes of the oblate particles are spherical [Fig. 9(c)]. The prolate particles are assumed to rotate in one plane, so that the corresponding excluded volume of a particle has a shape of an oblate ellipsoid [Fig. 9(d)]. These ellipsoidal excluded volumes are oriented randomly; for clarity of representation, all the volumes in the cartoon are shown to have their polar axis at either 0^o or 90^o to the image plane.